

# Evidence for Superconductivity at Ambient Temperature and Pressure in Nanostructures

Dev Kumar Thapa<sup>1</sup> and Anshu Pandey<sup>1\*</sup>

## Affiliations:

<sup>1</sup>Solid State and Structural Chemistry Unit, Indian Institute of Science, Bangalore 560012

\*Correspondence to: anshup@iisc.ac.in

**Despite being a low temperature phenomenon till date, superconductivity has found numerous applications in diverse fields of medicine, science and engineering. The great scientific interest in the phenomenon as well as its practical utility has motivated extensive efforts to discover and understand new superconductors. We report the observation of superconductivity at ambient temperature and pressure conditions in films and pellets of a nanostructured material that is composed of silver particles embedded into a gold matrix. Specifically, we observe that upon cooling below 236 K at ambient pressures, the resistance of sample films drops below  $10^{-4}$  Ohm, being limited by instrument sensitivity. Further, below the transition temperature, samples become strongly diamagnetic, with volume susceptibilities as low as -0.056. We further describe methods to tune the transition to temperatures higher than room temperature.**

While superconductivity was initially studied in metals such as lead<sup>1</sup>, more recently, materials as diverse as cuprates<sup>2,3</sup>, iron oxypnictides<sup>4,5</sup>, bismuth<sup>6,7</sup>, graphene<sup>8</sup> and even H<sub>2</sub>S<sup>9</sup> have been shown to undergo transitions to superconducting states under suitable conditions. Despite the discovery of a large number of materials that undergo normal to superconducting transitions, it is apparent that conditions of extremely low temperature and/or extremely high pressure are necessary in each case<sup>9-17</sup>. Therefore, there remains an unfulfilled need for a material system that undergoes this transition under more conveniently attainable temperature and pressure conditions.

Nanostructured materials have been extensively investigated in the context of superconductivity<sup>18-27</sup>. For example, recent studies have shown that nanostructuring gives rise to enhancements in critical magnetic fields of lead<sup>24,25,28</sup>. More significantly, some past studies showed modest increases in transition temperatures in the case of certain nanostructured materials over their bulk counterparts<sup>29</sup>. In all such investigations, the nanostructured material was also known to undergo a superconducting transition in its bulk form<sup>1</sup>. The explanations of transition temperature rise were based on extensions of the BCS formalism<sup>30</sup> as well as more unconventional pictures such as polarization waves and plasmons<sup>21,31-36</sup>.

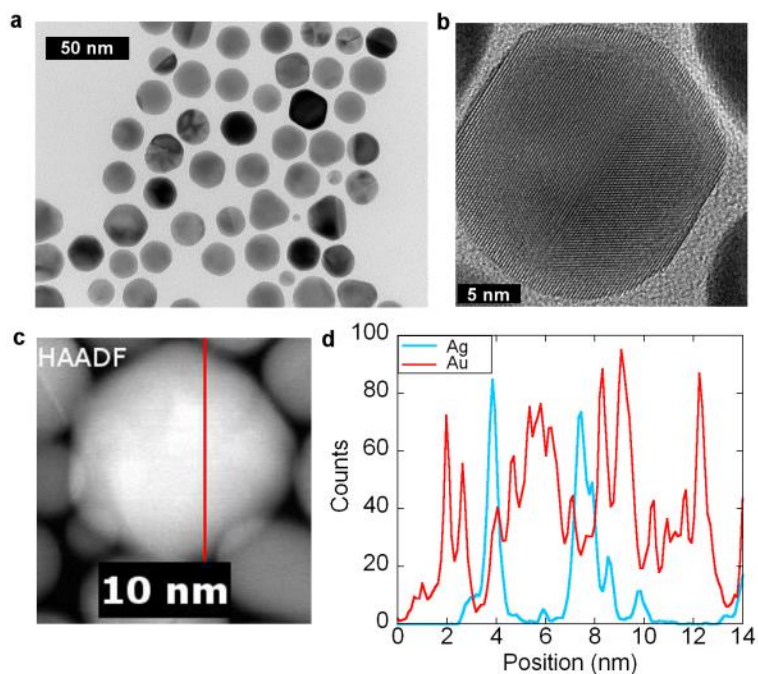


**Figure 1.** Structural characterization of NS prepared in this work. **(a)** TEM image of NSs. **(b)** HRTEM image of a single NS. **(c)** HAADF-STEM map of a single NS. **(d)** The elemental distribution along the red line in panel (c).

With a view towards discovering non-phonon based electron pairing mechanisms (*viz.* plasmonic)<sup>37-40</sup>, we investigated the properties of nanostructures prepared from Au and Ag. Both materials have low electron-phonon coupling and are not known to exhibit a superconducting state independently. During our studies we synthesized nanostructures (NS) comprising of silver particles (~1 nm) embedded into a gold matrix. Sample preparation was done using standard colloidal techniques. Briefly, the method employed by us involves the preparation of silver particles (exemplified in figure S1) that are then incorporated into a gold matrix in a separate, second step. Figure 1a and 1b shown a representative transmission electron microscopy (TEM) image and a high resolution TEM (HRTEM) image of the resultant particles. The lattice planes observed in figure 1b correspond to the [111] plane of Au and Ag. Due to the near identical lattice constants of both constituents, lattice diffraction methods lead to a single diffraction maximum for each material. Figure S2a additionally shows the ensemble X-ray diffraction pattern of the material. The ensemble level reflections are also in excellent agreement to the standard powder patterns of either Au or Ag. To better understand their internal structure, we studied these NS using electron microscopy. Images were recorded using a 200 kV Titan TEM (Thermo Fisher Scientific), and samples were deposited on a carbon coated grid in each case. Figure 1c shows a HAADF-elemental contrast image of these nanostructures. The elemental occurrences of silver and gold along the red line are shown in Figure 1d. Figures S2b-e further exemplify the elemental occurrences within these NS. Figure S3 additionally shows the overall

compositional analysis of the material using energy dispersive x-ray spectroscopy (EDAX). Collectively, these data confirm the successful inclusion of silver particles into the gold matrix.

These nanostructures were cast into films or else compacted into pellets for further study. Figure 2 exemplifies the typical electrical properties observed in these nanostructured materials. Granular superconductors with discrete particles may or may not show the transition in resistivity measurements, depending on the precise state of separation of particles and their electrical properties in the normal state.<sup>41</sup> Consequently, we employed the methods described in the extended data to ensure the sintering of particles (effects of chemical sintering are highlighted in Figure S4). The data in figure 2a were collected by depositing a 25 nm thick layer (Figure S5) of the nanocrystals onto a four-probe electrode (Figure S6) comprising of four 100 nm high gold fingers evaporated onto a glass substrate. In the region of sample deposition, the spacing between fingers 100  $\mu\text{m}$ , while each digit is 1 mm thick. As is evident from the data shown in figure 2a, the resistance of the sample is weakly temperature sensitive until it abruptly falls below  $10^{-4}$  ohm at temperatures lower than 240 K. Using the Nelson-Halperin formulation ( $R \propto \sinh^{-2}(C/\sqrt{T - T_c})$ ) that is applicable to the Berezinskii-Kosterlitz-Thouless transition in thin superconducting films,<sup>42</sup> we obtain a transition temperature of  $T_c = 236 \text{ K}$  for the system. To obtain this temperature, data points in the vicinity of the transition were fit to the above expression. The value of  $10^{-4}$  ohm is essentially limited by the instrument characteristics, and corresponds to a resistivity  $< 10^{-10}$  ohm-m, well below the resistivity of any known normal material. We further studied the effects of magnetic field on this transition. Consistent with the expectations of a normal to superconducting transition, the transition temperature decreases with increasing fields. This effect is shown in Figure 2b. It is further noteworthy that above the transition temperature, resistance of this sample is magnetic field independent and rises roughly linearly with temperature (Figure S7).

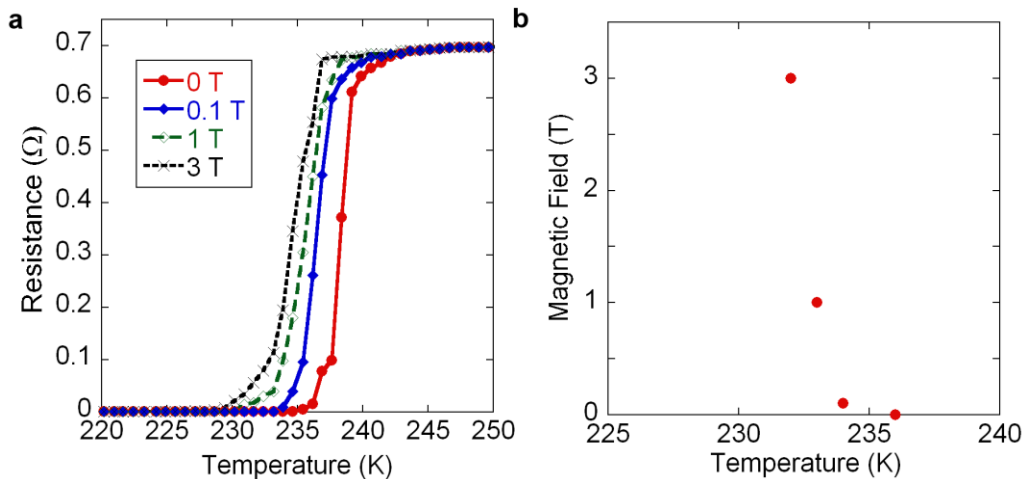


**Figure 2.** (a) Variation of resistance of a 25 nm thick film of NSs with temperature at different fields. (b) Relationship of  $T_c$  and magnetic field for the data in panel (a).

Besides the transition in resistance, the appearance of strong diamagnetism is also observed when this sample is cooled. This is highlighted in figure 3a that shows the zero field cooled (ZFC) susceptibilities of a pellet of the sample. Consistent with the results obtained from films, pellets of this sample also show a sharp decrease in susceptibility at 234 K. The slight difference in the transition temperatures of the pellet and the film could arise from the different processing schemes employed to make a film and a pellet as well as due to geometry effects. Regardless, 65 mg of this sample with a density of 11.61 g/cc shows volume susceptibilities as low as -0.056 (SI units) that are about a fifth of what we observe in the case of a 90 mg pellet of lead at 5 K, using the same measurement protocols (see extended data). Our inability to attain a perfect ( $\chi_v = -1$ ) diamagnetic state in this class of materials presumably arises due to imperfect sintering and the continued persistence of the nanoparticles within the material. The diamagnetic response of a granular superconductor composed of nanoparticles of radius  $r$  is given by  $\chi_v = -\frac{3}{20} \frac{r^3}{\lambda_L^2 \xi_0}$ , where  $\chi_v$  is the volume susceptibility,  $\lambda_L = 22 \text{ nm}$  is the London penetration depth and  $\xi_0 = 45 \text{ nm}$  is the coherence length<sup>43</sup>. Indeed, the magnitude of the observed diamagnetism is thus consistent with a granular superconductor of grain size 20 nm. This grain size estimate is in good agreement with the topography observed in sintered nanoparticle assemblies exemplified by figure S5 (mean grain size  $\sim 30 \text{ nm}$ ). Further, the observed diamagnetism is far stronger than the values associated with most normal materials, as well as with previous reports of nanostructured gold or silver. Figure 3b further shows the variation of  $T_c$  with applied magnetic field.

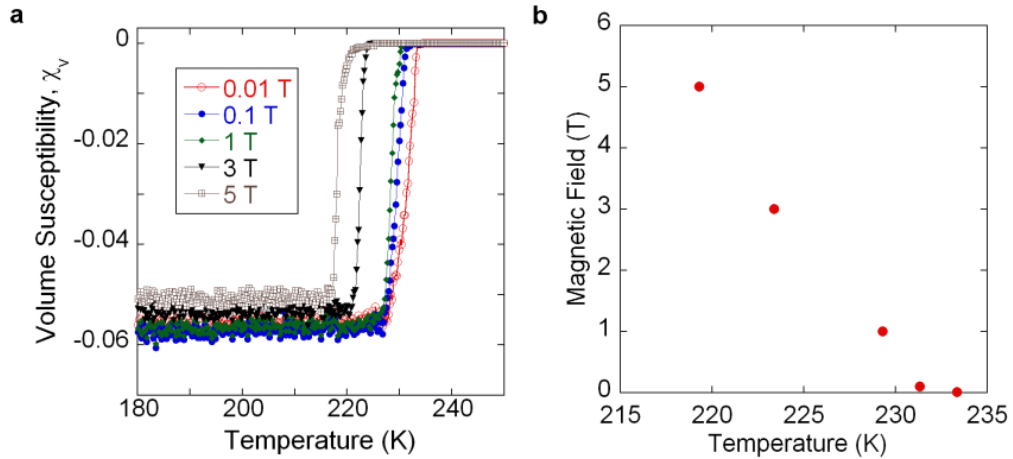


**Figure 3.** (a) Variation of volume magnetic susceptibility of a pellet of NSs with temperature at different fields. (b) Relationship of  $T_c$  and applied magnetic field for data in panel (a).

We further studied the variation of the superconducting transition temperature as a function of the material composition. In particular, Figure S8 shows the transition of three different samples containing different Au and Ag mole fractions. In each case the stoichiometric

ratio has been altered by growing different amounts of Au over the same Au/Ag core. Figure 4a further shows the variation of the transition temperature plotted against the Au mole fraction in the NS. As evident from this figure, increased Au mole fraction on the NS significantly lowers the transition temperature. In view of this observation, we focused our attention towards NSs with a low Au mole fraction, prepared by limiting Au overgrowth in the synthetic steps.

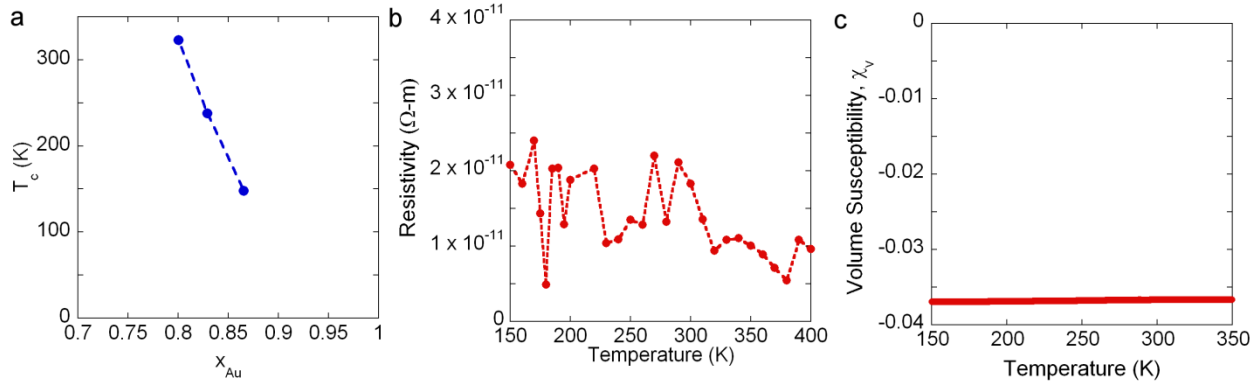


**Figure 4.** (a) Variation of  $T_c$  with composition for a single starting NS core. (b) Resistivity and (c) Susceptibility for NS with low Au mole fraction.

Films of NSs with low Au mole fraction ( $x_{Au} = 0.73$ ) were prepared using procedures that will be reported elsewhere. Figure 4b shows the typical resistivity of a 25 nm thick film of such NSs. While a measurable transition could not be observed in the temperature window accessible to us, it is nevertheless apparent that the sample resistivity ( $\sim 10^{-11} \Omega - m$ ) is significantly lower than the bulk resistivity of highly conductive metals such as Au and Ag ( $\sim 10^{-8} \Omega - m$  over a similar measurement range). Further, we observed that pellets of such samples are significantly diamagnetic ( $\chi_v = -0.037$ ) under ambient conditions (Figure 4d), consistent with the existence of a superconducting state at room temperatures.

## Conclusions

In conclusion, we describe observations that strongly suggest the emergence of superconductivity in an Au-Ag based material at ambient temperature and pressure conditions. We observed the transitions in magnetic susceptibility as well as resistance upon cooling the samples below 236 K (-37 °C) at ambient pressures. The transition temperature was observed to shift to lower temperatures at applied magnetic fields. The transition temperature could be tuned by varying the NS architecture, allowing us to observe transitions in resistivity at temperatures higher than room temperature. We further described the preparation of samples where a strongly diamagnetic, highly conductive state appears to persist over the temperature range available to us. Our observations pave the way for the fabrication of devices of these NS capable of room temperature operation.

## Acknowledgements:

AP acknowledges the Indian Institute of Science for funding. We thank Prof. Satish Patil for allowing us to use their laboratory equipment acquired under a Swarnajayanti Fellowship. We further thank CENSE for access to their facilities. Additionally, we thank Prof. Naga Phani Aetukuri and Prof. Vijay Shenoy for helpful discussions. DKT thanks Mr. Subham Kumar Saha for help with synthesis and measurements.

## References:

- 1 Boorse, H. A., Cook, D. B. & Zemansky, M. W. Superconductivity of Lead. *Phys. Rev.* **78**, 635-636, (1950).
- 2 Bednorz, J. G. & Müller, K. A. Possible high  $T_c$  superconductivity in the Ba–La–Cu–O system. *Zeitschrift für Physik B Condensed Matter* **64**, 189-193, (1986).
- 3 Chu, C. W. *et al.* Superconductivity above 150 K in  $\text{HgBa}_2\text{Ca}_2\text{Cu}_3\text{O}_{8+\delta}$  at high pressures. *Nature* **365**, 323, (1993).
- 4 Kamihara, Y. *et al.* Iron-Based Layered Superconductor:  $\text{LaOFeP}$ . *J. Am. Chem. Soc.* **128**, 10012-10013, (2006).
- 5 Kamihara, Y., Watanabe, T., Hirano, M. & Hosono, H. Iron-Based Layered Superconductor  $\text{La}[\text{O}_{1-x}\text{F}_x]\text{FeAs}$  ( $x = 0.05\text{--}0.12$ ) with  $T_c = 26$  K. *J. Am. Chem. Soc.* **130**, 3296-3297, (2008).
- 6 Prakash, O., Kumar, A., Thamizhavel, A. & Ramakrishnan, S. Evidence for bulk superconductivity in pure bismuth single crystals at ambient pressure. *Science* **355**, 52-55, (2017).
- 7 Tian, M. *et al.* Observation of Superconductivity in Granular Bi Nanowires Fabricated by Electrodeposition. *Nano Lett.* **6**, 2773-2780, (2006).
- 8 Cao, Y. *et al.* Unconventional superconductivity in magic-angle graphene superlattices. *Nature* **556**, 43, (2018).
- 9 Drozdov, A. P., Eremets, M. I., Troyan, I. A., Ksenofontov, V. & Shylin, S. I. Conventional superconductivity at 203 kelvin at high pressures in the sulfur hydride system. *Nature* **525**, 73, (2015).
- 10 Akimitsu, J. & Muranaka, T. Superconductivity in  $\text{MgB}_2$ . *Physica C: Superconductivity* **388-389**, 98-102, (2003).
- 11 Singleton, J. & Mielke, C. Quasi-two-dimensional organic superconductors: A review. *Contem. Phys.* **43**, 63-96, (2002).
- 12 Varma, C. M., Zaanen, J. & Raghavachari, K. Superconductivity in the Fullerenes. *Science* **254**, 989, (1991).
- 13 Shi, W. *et al.* Superconductivity in Bundles of Double-Wall Carbon Nanotubes. *Sci. Rep.* **2**, 625, (2012).
- 14 Tang, Z. K. *et al.* Superconductivity in 4 Angstrom Single-Walled Carbon Nanotubes. *Science* **292**, 2462, (2001).
- 15 Ekimov, E. A. *et al.* Superconductivity in diamond. *Nature* **428**, 542, (2004).
- 16 Steglich, F. *et al.* Superconductivity in the Presence of Strong Pauli Paramagnetism:  $\text{CeCu}_2\text{Si}_2$ . *Phys. Rev. Lett.* **43**, 1892-1896, (1979).
- 17 Petrovic, C. *et al.* Heavy-fermion superconductivity in  $\text{CeCoIn}_5$  at 2.3 K. *J. Phys.: Condens. Matter.* **13**, L337, (2001).

- 18 Beloborodov, I. S., Lopatin, A. V., Vinokur, V. M. & Efetov, K. B. Granular electronic systems. *Rev. Mod. Phys.* **79**, 469-518, (2007).
- 19 Christophe, B., Tristan, C. & Dimitri, R. Review of 2D superconductivity: the ultimate case of epitaxial monolayers. *Supercond. Sci. Technol.* **30**, 013003, (2017).
- 20 Croitoru, M. D., Shanenko, A. A., Kaun, C. C. & Peeters, F. M. Ultra-small metallic grains: effect of statistical fluctuations of the chemical potential on superconducting correlations and vice versa. *J. Phys. Condens. Matter* **24**, 275701, (2012).
- 21 Hurault, J. P. Superconductivity in small crystallites. *J. Phys. Chem. Solids* **29**, 1765-1772, (1968).
- 22 Jiepeng, L., Xuefeng, W., Fangfei, M., Kedong, W. & Xudong, X. Superconductivity of individual Pb islands on Si(111): pseudogap, critical region, density of states, and island size. *Supercond. Sci. Technol.* **26**, 085009, (2013).
- 23 Zgirski, M., Riikonen, K.-P., Touboltsev, V. & Arutyunov, K. Size Dependent Breakdown of Superconductivity in Ultranarrow Nanowires. *Nano Lett.* **5**, 1029-1033, (2005).
- 24 He, M. *et al.* "Giant" Enhancement of the Upper Critical Field and Fluctuations above the Bulk  $T_c$  in Superconducting Ultrathin Lead Nanowire Arrays. *ACS Nano* **7**, 4187-4193, (2013).
- 25 Dickey, J. M. & Paskin, A. Phonon Spectrum Changes in Small Particles and Their Implications for Superconductivity. *Phys. Rev. Lett.* **21**, 1441-1443, (1968).
- 26 Yung-Jung, H., Shih-Yuan, L. & Yi-Feng, L. Nanostructures of Sn and Their Enhanced, Shape-Dependent Superconducting Properties. *Small* **2**, 268-273, (2006).
- 27 Sangita, B. & Pushan, A. A review of finite size effects in quasi-zero dimensional superconductors. *Rep. Prog. Phys.* **77**, 116503, (2014).
- 28 Zolotavin, P. & Guyot-Sionnest, P. Superconductivity in Films of Pb/PbSe Core/Shell Nanocrystals. *ACS Nano* **6**, 8094-8104, (2012).
- 29 Hauser, J. J. Enhancement of Superconductivity in Aluminum Films. *Phys. Rev. B* **3**, 1611-1616, (1971).
- 30 Bardeen, J., Cooper, L. N. & Schrieffer, J. R. Microscopic theory of superconductivity. *Phys. Rev.* **106**, 162-164, (1957).
- 31 Kohn, W. & Luttinger, J. M. New Mechanism for Superconductivity. *Phys. Rev. Lett.* **15**, 524-526, (1965).
- 32 Giuliani, G. F. Plasmon mechanism for superconductivity in semiconducting heterostructures: The effect of acoustic plasmons. *Surf. Sci.* **196**, 476-481, (1988).
- 33 Eliashberg, G. M. Temperature Green's Function for Electrons in a Superconductor. *JETP* **12**, 1000, (1960).
- 34 Eliashberg, G. M. Interactions between Electrons and Lattice Vibrations in a Superconductor. *JETP* **11** 966, (1959).
- 35 Migdal, A. B. Interaction between electrons and lattice vibrations in a normal metal. *JETP* **7**, 996, (1958).
- 36 Mahan, G. D. & Wu, J.-W. Plasmons and high-temperature superconductivity. *Phys. Rev. B* **39**, 265-273, (1989).
- 37 Di Bernardo, A. *et al.* p-wave triggered superconductivity in single-layer graphene on an electron-doped oxide superconductor. *Nat. Commun.* **8**, 14024, (2017).
- 38 Ott, H. R., Rudigier, H., Fisk, Z. & Smith, J. L.  $UBe_{13}$ : An Unconventional Actinide Superconductor. *Phys. Rev. Lett.* **50**, 1595-1598, (1983).
- 39 Krasnov, V. M., Katterwe, S.-O. & Rydh, A. Signatures of the electronic nature of pairing in high- $T_c$  superconductors obtained by non-equilibrium boson spectroscopy. *Nat. Commun.* **4**, 2970, (2013).
- 40 Okazaki, K. *et al.* Evidence for a  $\cos(4\phi)$  Modulation of the Superconducting Energy Gap of Optimally Doped  $FeTe_{0.6}Se_{0.4}$  Single Crystals Using Laser Angle-Resolved Photoemission Spectroscopy. *Phys. Rev. Lett.* **109**, 237011, (2012).

- 41 Jaeger, H. M., Haviland, D. B., Orr, B. G. & Goldman, A. M. Onset of superconductivity in ultrathin granular metal films. *Phys. Rev. B* **40**, 182-196, (1989).
- 42 Halperin, B. I. & Nelson, D. R. Resistive transition in superconducting films. *J. Low Tem. Phys.* **36**, 599-616, (1979).
- 43 Zolotavin, P. & Guyot-Sionnest, P. Meissner Effect in Colloidal Pb Nanoparticles. *ACS Nano* **4**, 5599-5608, (2010).



## Supplementary Information

### Evidence for Superconductivity at Ambient Temperature and Pressure in Nanostructures

Dev Kumar Thapa<sup>1</sup> and Anshu Pandey<sup>1\*</sup>

<sup>1</sup>Solid State and Structural Chemistry Unit, Indian Institute of Science, Bangalore 560012

\*Correspondence to: anshup@iisc.ac.in

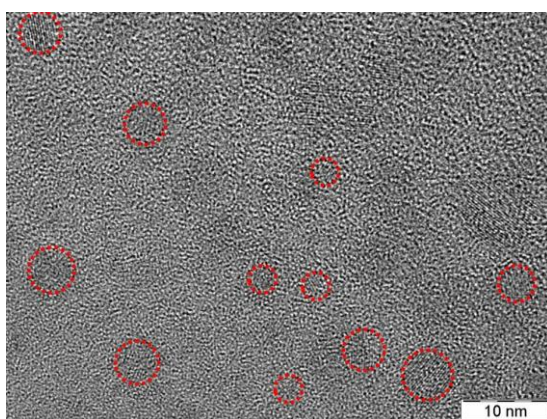


**Figure S1.** TEM image of small (~1 nm) Ag particles

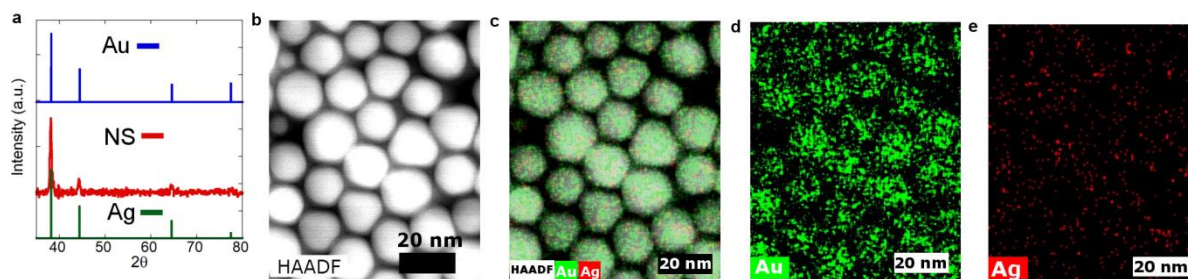


**Figure S2.** Structural characteristics of the NSs. (a) Powder XRD pattern of NS (red) matches with the standard pattern of gold (blue). (b) - (e) HAADF-STEM of the NS with elemental mapping.

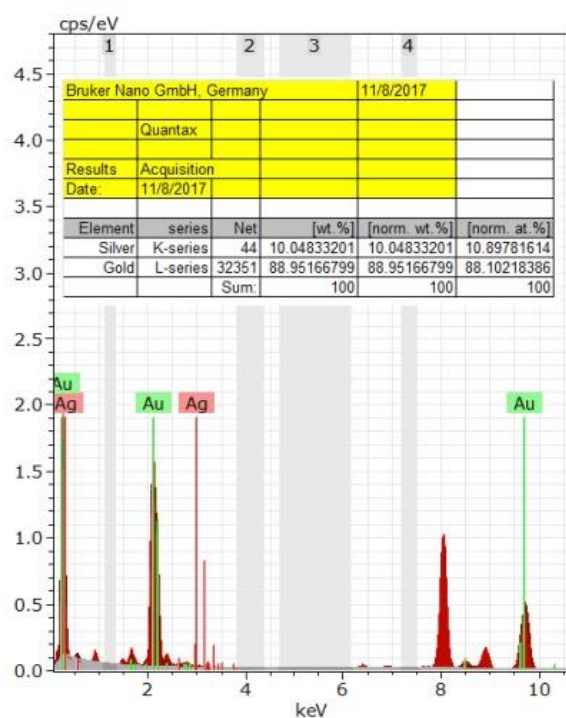


**Figure S3.** Energy Dispersive X-Ray spectrum and elemental composition of the NS.

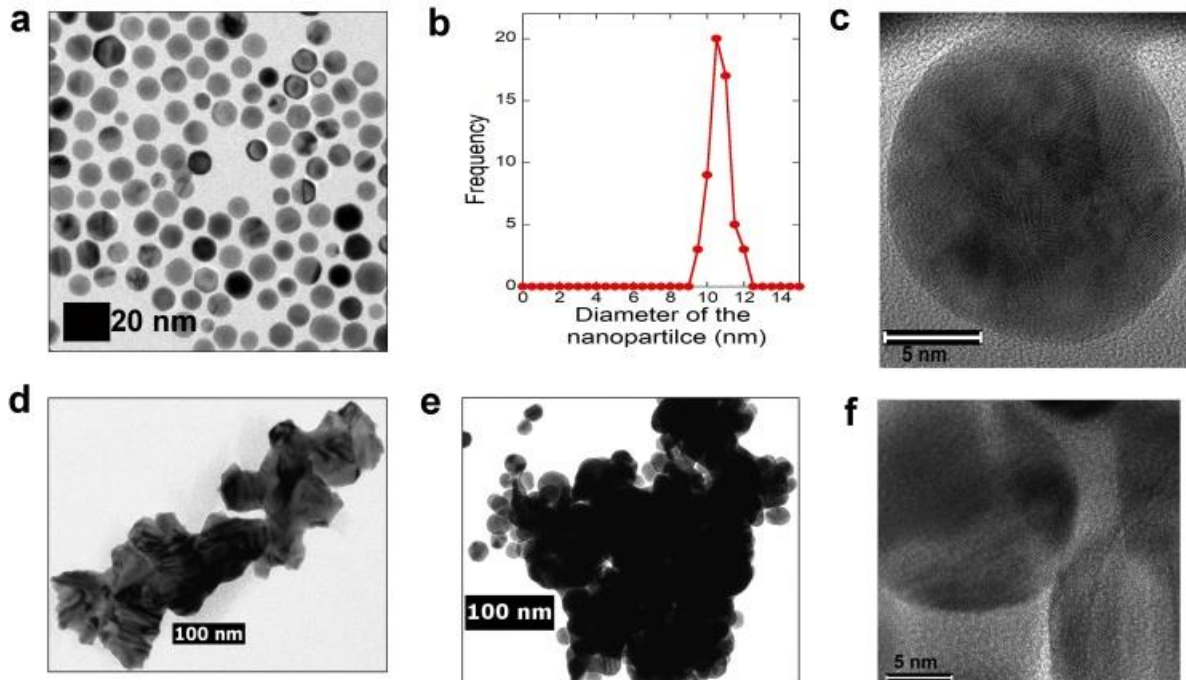


**Figure S4.** TEM and HRTEM images of NS. (a) TEM images of NS. (b) Size distribution corresponding to panel (a). (c) HRTEM image of the NS. (d)-(e) TEM images of agglomerated NS and (f) HRTEM image of agglomerated NS. To acquire (d)-(e) the sintered NS were sonicated in water for 2 hours, the dispersed particles were then drop cast onto a carbon coated copper grid for microscopic imaging.

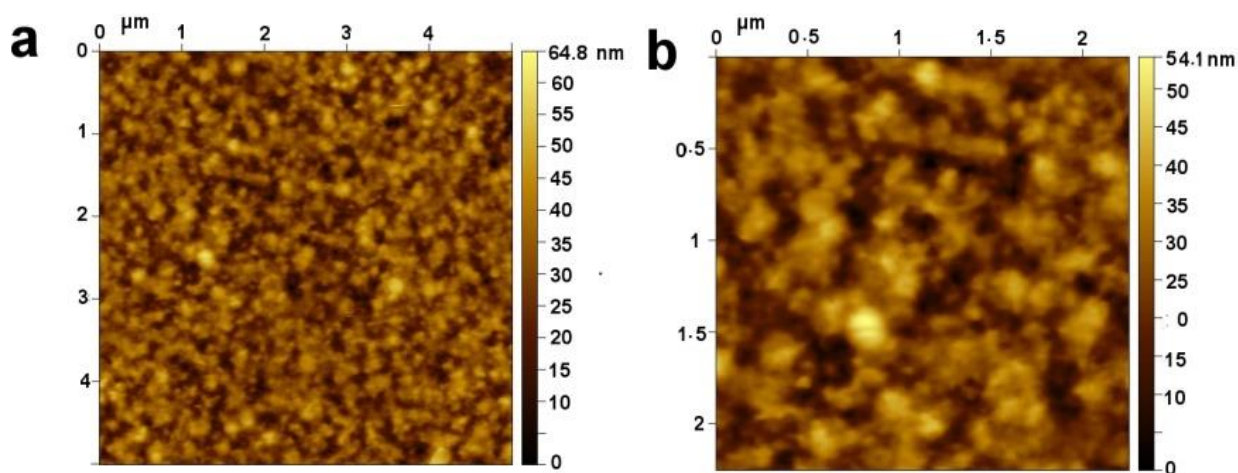


**Figure S5.** AFM image a deposited NS film used to study electrical characteristics.

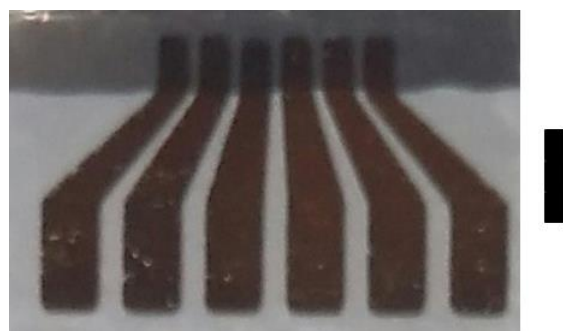


**Figure S6.** Optical image of the electrode array on a glass substrate. The dark gray region is the deposited sample. Each Au digit has a 1 mm width in the region of the sample deposition. The inter-digit gap is 100  $\mu\text{m}$  and each digit is 100 nm high. Scale bar: 3 mm.

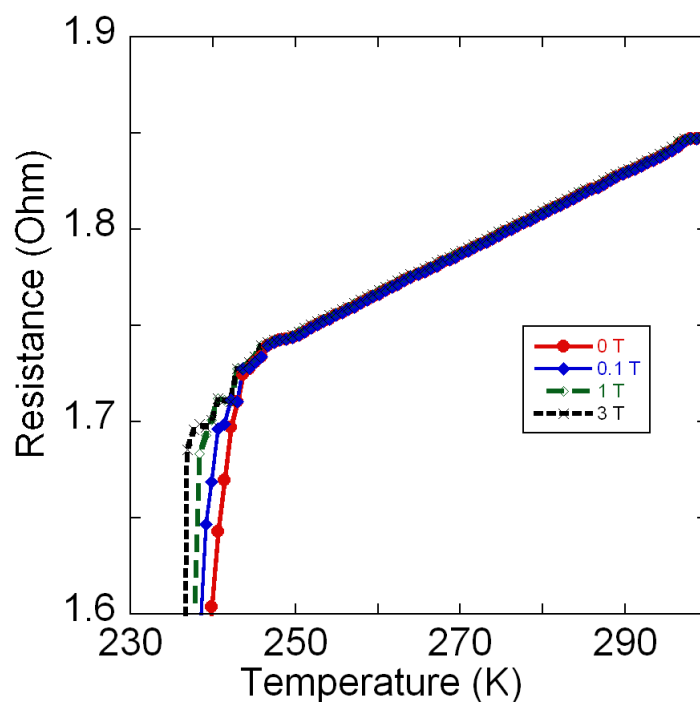


**Figure S7.** Variation of sample resistance above the transition temperature. Resistance is observed to increase roughly linearly, independent of applied magnetic field.

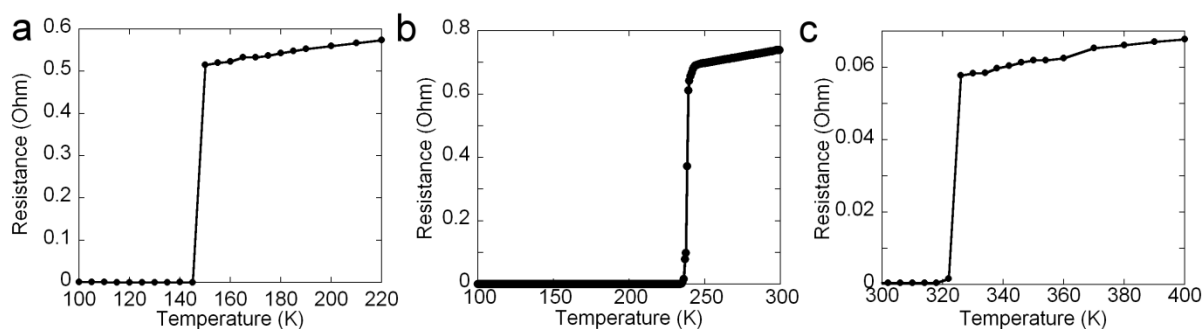


**Figure S8.** Transitions in resistivity as observed for three different NS samples.

### Experimental procedures:

**TEM characterization:** TEM grid was prepared with ultra clean sample in water solution. HR-TEM images were obtained on a Themis TITAN transmission electron microscope (200 kV). STEM was performed in a Themis TITAN TEM operating at 200 kV. STEM-EDX elemental mapping was also performed using the same instrument.

**Magnetic susceptibility measurement:** The obtained fine grains were separated from the growth solution, dried and a pellet was made by pressing in a titanium die. The obtained pellet which weight 65 mg was taken for magnetometry measurement. The magnetometry measurement was done in a SQUID (MPMS<sup>®</sup>3, Quantum Design). The sample was filled into

a tube that was then attached to the sample holder. The holder was placed on SQUID and various measurements were taken.

**Resistance measurement:** For resistivity measurement the film was prepared as follows. A partially cleaned sample was drop casted on a glass substrate which had six gold metallic pads (100 nm height with a width of 1 mm and an equidistant separation of 100  $\mu\text{m}$ ) deposited on it. The cross linking was done by adding  $\text{CHCl}_3$  followed by KOH (aqueous). Only four of the electrodes were employed during the actual measurement. The process of addition of  $\text{CHCl}_3$  followed by KOH (aqueous) was repeated twice. After each addition the film was washed with water several times. The film was dried in vacuum inside a desiccator and moved to Glove-box immediately after drying. The film was blown with Nitrogen gas prior to the measurement. Film thickness was verified using optical profilometry as well as through atomic force microscopy (Cypher ES, Asylum Research). The measurement was carried out in PPMS6000 from quantum design and four probe measurement setup from Agilent Technologies.